# Improved mm-wave interferometry for kinetic inductance detectors

A. Fasano[1],[*], M. Aguiar[3], A. Benoit[1], A. Bideaud[1], O. Bourrion[2], M. Calvo[1], A. Catalano[2], A. P. de Taoro[3], G. Garde[1], A. Gomez[4], M. F. Gomez Renasco[3], J. Goupy[1], C. Hoarau[2], R. Hoyland[3], J. F. Macías-Pérez[2], J. Marpaud[2], A. Monfardini[1], G. Pisano[6], N. Ponthieu[5], J. A. Rubiño Martín[3], D. Tourres[2], C. Tucker[6], A. Beelen[7], G. Bres[1], M. De Petris[4], P. de Bernardis[4], G. Lagache[7], M. Marton[2], R. Rebolo[3], and S. Roudier[2]

[1] Institut Néel, CNRS and Université Grenoble Alpes, France
[2] Laboratoire de Physique Subatomique et de Cosmologie, Université Grenoble Alpes, CNRS/IN2P3, 53, avenue des Martyrs, Grenoble, France
[3] Instituto de Astrofsica de Canarias, C/Va Lctea s/n, E-38205 LaLaguna, Tenerife, Spain
[4] Dipartimento di Fisica, Sapienza Università di Roma, Piazzale Aldo Moro 5, I-00185 Roma, Italy
[5] Univ. Grenoble Alpes, CNRS, IPAG, F-38000 Grenoble, France
[6] Astronomy Instrumentation Group, University of Cardiff, UK
[7] Aix Marseille Université, CNRS, LAM (Laboratoire d'Astrophysique de Marseille) UMR 7326, 13388, Marseille, France

**Abstract**

*Context.* Major features demanded for instruments in contemporary cosmology are: high mapping speed to cover large portion of the sky and multi-frequency capability for the component separation. In order to simultaneously satisfy the two conditions you can design large arrays of photo noise limited detectors adopting a spectroscopy technique that allows wide instantaneous Field of View (FoV). In this framework we developed KISS (KIDs- Interferometer-Spectrum-Survey), a spectrometric-imager dedicated to the secondary anisotropies of the Cosmic Microwave Background Radiation (CMBR). In particular the instrument aims to observe the Sunyaev Zel'dovich effect (SZ): an effect due to the interaction between the cluster of galaxies and the CMBR.
*Method.* We exploit a Fourier Transform Spectrometer (FTS): instead of distribute the pixels to the different frequencies (e.g. on-chip and grating spectroscopy) we developed a dual arrays sensitive to all the interested band. Thanks to the FTS we can separate and reconstruct the spectrum. In the ground-based case like KISS, the drawback from such a technique is represented by the necessity to avoid signal contamination from the atmospheric background fluctuations. The single interferometric figure must be acquired with a stable background to properly convert it in a spectrum where the noise does not become indistinguishable from the signal. It is, thus, necessary to use low time-constant detectors and fast FTS technology. KISS adopts, for such target, two arrays of Kinetic Inductance Detector (KID).
*Aims.* In this paper we describe the solution adopted to improve the calibration accuracy of the instrument.
*Results.* We first demonstrate the feasibility of this technique with a simulation. We, then, study the performance of such technique for the modulation and the tuning, applying it to real on-sky observations. The acquisition technique has been qualified during the commissioning campaign during Summer 2019 in Tenerife. It represents a solution for fast multi-frequency acquisition experiments exploiting KID based interferometer.

**Key words.** Keywords should be given

## 1. Introduction

Foregrounds subtraction and components separation in mm-wavelengths astronomy require simultaneous observation at different frequencies. This scenario suggests the choice of FTS: this technique exploits the interference of light rather than separate the wavelengths and, compared to competitors (on-chip (Endo et al. (2012)) and grating (Li et al. (2018)) spectroscopy), allows larger instantaneous FoV.

KISS is a fast spectrometer based on KID (for an overview see Zmuidzinas (2012)) and installed at the 2.25 m QUIJOTE telescope (see Fasano (submitted-b) and Fasano (submitted-a) for the instrument description). Firstly, as in the past for FIRAS (Mather et al. (1999)), the selection of the FTS for the will of developing an instrument fells on a Martin Puplett: an interferometer that measures the difference between the powers of two input beams (Martin & Puplett (1970)). The MPI transposes the ob-

serving frequencies paradigm from time to spacial domain and allows to use a calibration source: an ideal choice for precise measurements. Secondly, the necessity to go fast on data acquisition makes suitable to choose fast detectors like KID. Taking in consideration these premises, using a "brute-force" acquisition technique, where you just stock all the information available, would result on a huge data production. Starting from this scenario, it is desirable to adopt a smart solution that minimises the amount of data. In the case of dual band photometers, such as NIKA Monfardini et al. (2010) and NIKA2Adam et al. (2018), the acquisition rate at 23.48 Hz allows to average the points and obtain a calibration, for KISS the premises are different it is a ground-based spectrometer and it fast integrates to avoid atmospheric contamination. It cannot, thus, average because of the rapid background fluctuations.

In sec. 2 we describe the KID and we show the properties of KISS arrays. In sec. 3 we introduce the method used in past for NIKA2 for calibration and tuning. In the same section, it is described the new method for KISS, the data implementation and

the algorithm. In the sec. 4 we show two validation results: the the technique simulation of to demonstrate under which condition the method works. In the end, we apply the calibration to on-sky data.

## 2. KID properties

The KID a is high quality factor superconducting resonator, exploited as detector in millimetre wavelengths. It is based on the change of kinetic inductance with an incoming radiation, that is inversely proportional to the density of Cooper pairs. The absorbed power can be determined by measuring the change on the resonance frequency. It is read-out by a bias line injecting a tone at its correspondence resonant frequency; at this peculiar frequency, in fact, the coupling between the resonator and the readout line results in an energy absorption, aka band-stop filter. Its time constant is fixed by the recombination time of the quasi-particles (few $10\mu s$). This represents a major advantage with respect to competitors that are, indeed, a factor $\gtrsim 10$ slower.

The $S_{21}$ signal (output/input ratio) related to the KID detector is studied in the complex plane $(I, Q)$, where the resonance shape corresponds to a circle. The conversion of the $(I, Q)$ signal to absorbed optical power is one of the most difficult challenge using KIDs and it represents a different issue to readout, e.g., thermal detectors (bolometer, TES et cetera).

In order to characterise our pixels we use the standard resonator values: the resonance frequency ($f_0$), the internal quality factor ($Q_i$) and the coupling quality factor ($Q_c$). In order to fit the resonance it is possible to use the skewed Lorentzian profile Gao (2008):

$$|S_{21}(f)| = A + B(f - f_0) + \frac{C + D(f - f_0)}{1 + 4Q_{tot}^2 \frac{(f - f_0)^2}{f_0^2}} , \qquad (1)$$

where $A$, $B$, $C$ and $D$ are factors that do not influence the parameters under study. We can, thus, characterise the pixels. With eq. 1 we can extrapolate $Qi$ (Gao (2008)):

$$Q_i = \frac{Q_{tot}}{min(|S_{21}(f)|)} . \qquad (2)$$

In fig. 1 and 2 we show the electrical measurements for the KISS arrays performed in laboratory.
In terms of the previous parameters, the pixel design answers to the necessity of particular specifications: the resonance frequency ($f_0$) is in agreement with the amplifier working range and the coupling quality factor ($Q_c$) is coupled to the internal one ($Q_i$), that is related to background, to maximise the responsivity (as demonstrated in Gao (2008)).

## 3. Photometric response

### 3.1. 2-point modulation technique

Smart readout technique is required to properly study the signal and do not encounter huge amount of data. In the past, e.g. for NIKA, an innovative readout technique has been developed (see Calvo et al. (2013) for a detailed discussion): the 2-point modulation technique. The idea, as described in Catalano et al. (2014b) , has been to replace the standard fixed excitation (single frequency) tone with a modulated input based on two different frequencies separated by $f_{LO}$:
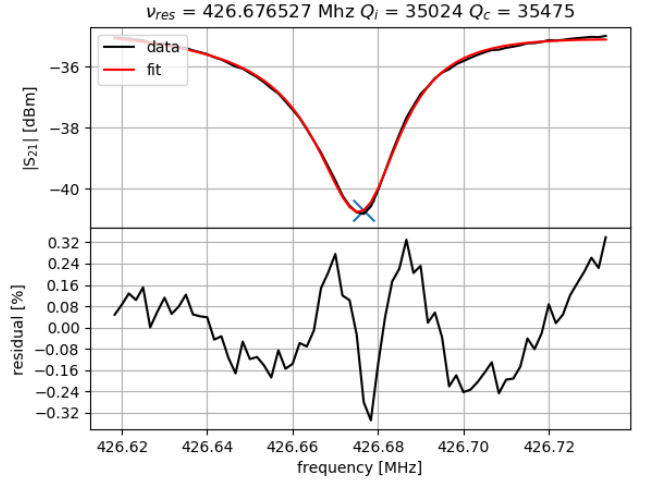


**Figure 1.** Up: single pixel bias signal data (in black) fitted (in red) by eq. 1. Bottom: percentile residual between fit and data.
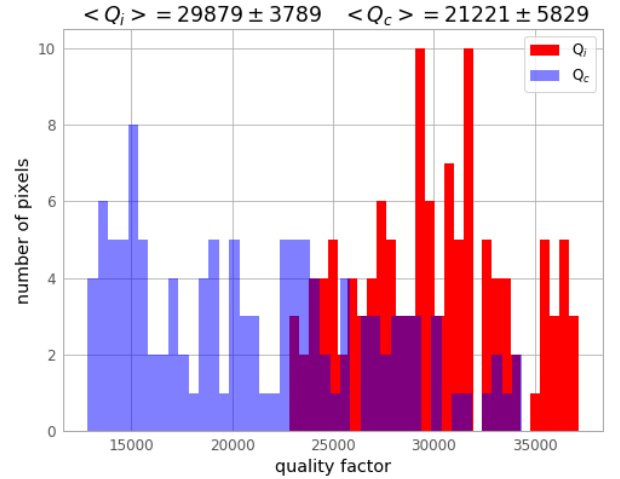


**Figure 2.** Quality factors histograms measured on the KISS array. In red the internal quality factor ($Q_i$) with a background of 50 K that simulates the sky and in blue the coupling quality factor ($Q_c$).

$$\begin{aligned} f_+ &= f_0 + \delta f_{LO}/2 , \\ f_- &= f_0 - \delta f_{LO}/2 , \end{aligned} \qquad (3)$$

where $f_0$ is the resonant frequency. This modulation is synchronised to the FPGA sampling of the signal at ~24 Hz. Each raw data point is composed by $(I(t), Q(t))$ values and the corresponding differential values:

$$\left(\frac{dI}{df}(t), \frac{dQ}{df}(t)\right) = \left(\frac{I(f_+) - I(f_-)}{\delta f_{LO}}, \frac{Q(f_+) - Q(f_-)}{\delta f_{LO}}\right) . \qquad (4)$$

In this way, if a variation $(\Delta I(t), \Delta Q(t))$ occurs between two successive points, it is possible to estimate the corresponding shift in the resonant frequency ($\Delta f_0(t)$) by projecting $(\Delta I(t), \Delta Q(t))$ along the gradient found, using eq. 4:

$$\Delta \hat{f}_0(t) = \frac{(\Delta I(t), \Delta Q(t)) \cdot (dI/df(t), dQ/df(t))}{(dI/df(t), dQ/df(t))^2} \cdot \delta f_{LO} \, , \quad (5)$$

we refer to $\Delta \hat{f}_0(t)$ as $RFdIdQ$.

The constraints over the data acquisition are slightly more demanding in KISS: two consecutive interferograms are acquired at 5 Hz, to overcome the 1/f atmospheric noise at ~1 Hz, and the data rate is quite higher (3.816 kHz) in order to obtain the aimed spectral resolution of few GHz. In this condition it is not possible to modulate each single point signal, because the FPGA does not reach the necessary rate and you would, eventually, manage a factor 2 on data weight.

### 3.1.1. Tuning procedure

The 2-point modulation technique, described in subsec. 3.1 is the major improvement on the data calibration and production. On the other side, to optimise the working point of the KID it is necessary to retune: while you observe, the atmospheric fluctuations modify the resonance. What is done at the end of each observation, in the standard perspective, is a full frequency sweep to retune the resonance frequency: this represents a time-demanding procedure. It is possible to adopt a strategy that permits to save ~75% of time in the pre-observation phase of retuning, this strategy is detailed explained in (Catalano et al. (2014a)). At first, you measure the angle $\Phi$ between the vectors $(I, Q)$ and $(dI/df_{LO}, dQ/df_{LO})$ referring to eq. 4 and you define, for convenience, a new angle $\theta \doteq \pi/2 - \Phi$ that changes smoothly around $[-\pi, \pi]$. Secondly, the excitation tone is fixed at $\theta = 0$ and you estimate the $\theta(f)$ slope $\Delta\theta/\Delta f'$. Then, you vary the tone frequency $f^i$ monitoring $\theta^i$. And finally, you can evaluate the new resonance frequency:

$$f_0^i \simeq f^i - \frac{\theta^i(t)}{\Delta\theta/\Delta f'} \, . \quad (6)$$

The procedure described in this section is a resilient tool that can be adopt on photometric KIDs-based experiments: even for large background fluctuations, you can iterate the algorithm to converge. As we will describe later, KISS adopts a different strategy.

### 3.2. 3-point modulation technique

As previously mentioned, we cannot use the same technique, described in the subsec. 3.1, for interferometry. The acquisition rate is not high enough to average successive interferogram points. The idea is, thus, to modulate the signal at the beginning of each interferogram.

### 3.2.1. Implementation

The spectral information is organised in data block containing forward and backward interferogram: a moving mirror oscillates generating the optical path difference that results in the interferogram figures, one per oscillation direction (see Fasano (submitted-b) for the detailed discussion). This repetitive points sequence is composed by a first part and second where there are injected two frequencies, respectively:

$$\begin{aligned} f_+ &= f_0 + \Delta f_{LO}/2 \, , \\ f_- &= f_0 - \Delta f_{LO}/2 \, , \end{aligned} \quad (7)$$

and for the rest the frequency of resonance $f_0$, as we can see in fig. 3.
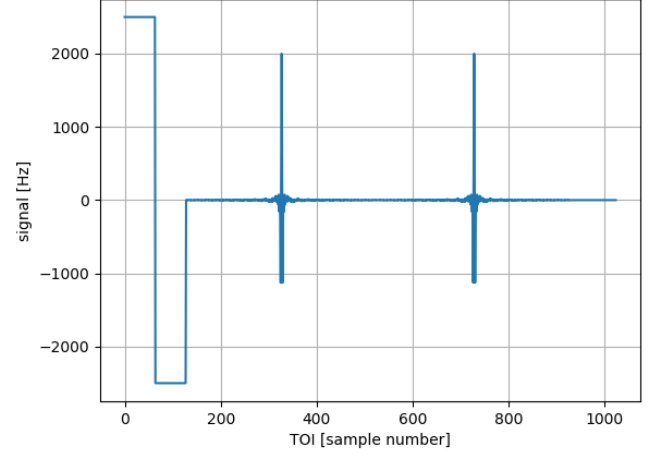


**Figure 3.** Data block simulation of KISS: signal [Hz] vs Time Ordered Information (TOI) [sample number]. There are a total of 1024 points: the first 128 dedicated to the modulation and the rest to incoming signal. We simulate the forward and backward interferograms with a typical amplitude of 2 kHz and input black body sources at 3 K and 30 K respectively.

The choice over the total number of points for one single block, including the ones assigned to the modulation, takes into account few major constraints: the spectral resolution aimed to ~1 GHz requires a displacement of the mirror of 10 cm; the cut-off of the KID time constant (few 10 $\mu$s), that limits the single datum acquisition rate; the fast (5 Hz) scan requirement to avoid the 1/f atmospheric noise. The result consists on a total period of 1024 points, where each point is acquired at 3.816 kHz, dedicating the first 128 to the modulation. In this way we have ~400 points each interferogram, obtaining ~100 points on the interested spectrum band (80÷300 GHz).

### 3.2.2. Calibration

We can extrapolate the calibration factor $C$ [Hz/rad] through a circular fit on the modulation points $(x_1, y_1)$ and $(x_2, y_2)$, and the baseline point $(x_3, y_3)$, referring to fig. 4.

We obtain, in this way, the coordinates of the circle centre $(I_c, Q_c)$. We can calculate, thus, the $r_1$ and $r_2$ angles as following:

$$\begin{aligned} r_1 &= \arctan\left(\frac{I_c - x_1}{Q_c - y_1}\right) \quad , \\ r_2 &= \arctan\left(\frac{I_c - x_2}{Q_c - y_2}\right) \quad . \end{aligned} \quad (8)$$

The calibration factor $C$ is, then, obtained by:

$$\begin{aligned} \Delta\phi &= r_2 - r_1 \quad , \\ C &= \Delta f_c/\Delta\phi \quad ; \end{aligned} \quad (9)$$

where $\Delta f_c$ is the modulation factor in hertz set by the injecting tone ($\Delta f_c = 2\Delta f_{LO}$ from eq. 7).

Operatively, $C$ converts the observing phase $\left(\phi = \arctan\left(\frac{I}{Q}\right)\right)$ to $f'$ hertz data. We first calculate the $r$ angle:
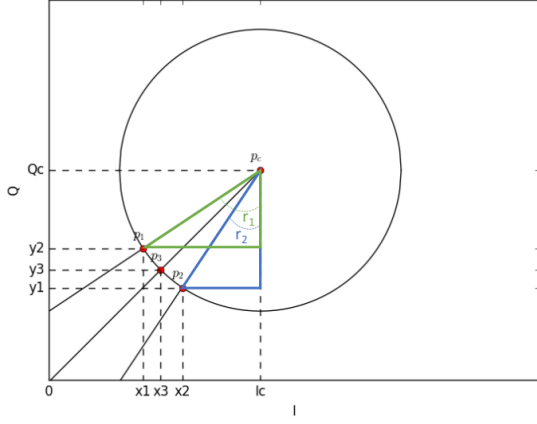
**Figure 4.** Resonance circle in the $(I, Q)$ plane. $p_1$ and $p_2$ are the modulation points, $p_3$ is the measurement point and $p_c$ is the circle centre.

$$r = \arctan\left(\frac{I_c - I}{Q_c - Q}\right). \qquad (10)$$

In the end, we obtain the frequency data:

$$f' = C \cdot r. \qquad (11)$$

This represents, indeed, the physical quantity that can be directly converted to incoming power (as seen in Swenson et al. (2010)).

## 4. Results

### 4.1. Validation with simulation

The first step to validate the calibration technique has been the simulation of the KID pixel used for KISS, qualifying it for the modulation technique. The $S_{21}$ signal of the KID resonator, in the complex plane is described by the equation (Gao (2008)):

$$S_{21}(f) = ae^{-2\pi jf\tau}\left[1 - \frac{\frac{Q_{tot}}{Q_c}e^{j\phi_0}}{1 + 2jQ_{tot}\left(\frac{f-f_0}{f_0}\right)}\right], \qquad (12)$$

where , $Q_{tot} \doteq (1/Q_i + 1/Q_c)^{-1}$ and $\Re$ is the responsivity measured during laboratory test; $\tau$ is the retard introduced by the cables and $\phi_0$ is a phase, and these last two parameters are not taken into account for this study.

**Table 1.** Input values from laboratory characterisation taken from the analysis showed in fig. 2 and discussed in subsec. 2.

| parameter | value |
|-----------|-------|
| $\tau$ | 1 |
| $\phi_0$ | 0 |
| $f_0$ | 500 MHz |
| $Q_i$ | 30'000 @ 50 K |
| $Q_c$ | 21'000 |
| $\Re$ | 1.5 kHz/K |

We can use, then, the eq. 12 inserting the laboratory values in tab. 1 to obtain the $S_{21}(f)$ simulated signal, whose module is shown in fig. 5.

First of all, starting from these simulated data we generate a data block with assigned modulation factor and interferogram
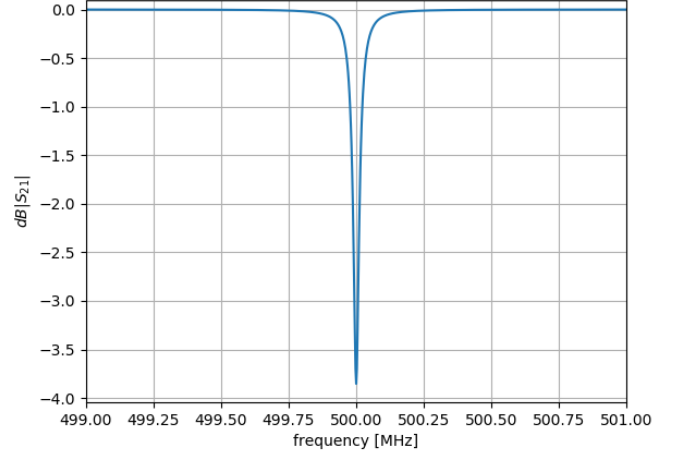


**Figure 5.** $|S_{21}|$ signal [dB] (simulated using eq. 12 with input values of tab. 1) vs frequency [MHz]. It represents the typical KISS pixel.

amplitude ($A$) in hertz. The second step is to use these hertz data with, again, eq. 12 obtaining the values in quadrature ($I, Q$). From them we compute the phase $\left(\phi = \arctan\left(\frac{I}{Q}\right)\right)$[1]. Finally we come back to hertz signal through the calibration algorithm described in subsec. 3.2.2. We, thus, compare the modulation factor and interferogram amplitude in input ($C_{in}$ and $A_{in}$) and output ($C_{out}$ and $A_{out}$) of this algorithm. This verification is necessary to understand the reliability of the calibration method. In fig. 6 we report the change of the calibration factor as a function of background, at fixed modulation factor and interferogram amplitude.
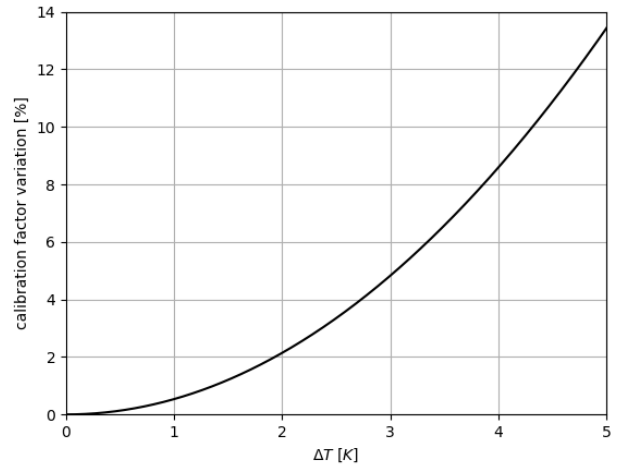


**Figure 6.** Calibration factor percentile variation $\left(\frac{C_{out}-C_{in}}{C_{in}}\right)$ vs background variation [K]. The modulation factor ($\Delta f_c$) is fixed at at 2.5 kHz. The calibration factor ($C_{out}$) is independent from $A_{in}$.

---

[1] $I = \Re(S_{21})$ and $Q = \Im(S_{21})$

In fig. 7 we show the variation on the estimation of the interferogram amplitude, at fixed modulation factor: we see how this estimation is degradated at large background variations.
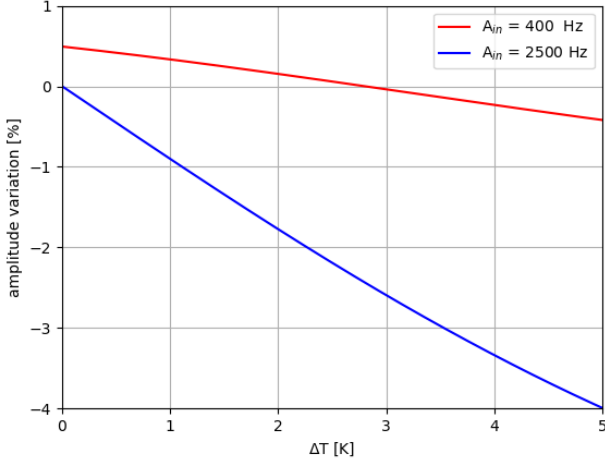


**Figure 7.** Interferogram amplitude percentile variation $\left(\frac{A_{out}-A_{in}}{A_{in}}\right)$ estimation vs background [K]. The modulation factor $(\Delta f_c)$ is fixed at 2.5 kHz. We can see how the higher value of the amplitude degrades the method.

In fig. 8 we show the last result of the simulation: every curve is at different, fixed interferogram amplitude and the figure represents the variation on the amplitude estimation in function of different calibration factors. As expected, we want to be as close as possible between the calibration factor and the amplitude variation. Other choices compromise the amplitude estimation of maximum ~1%.



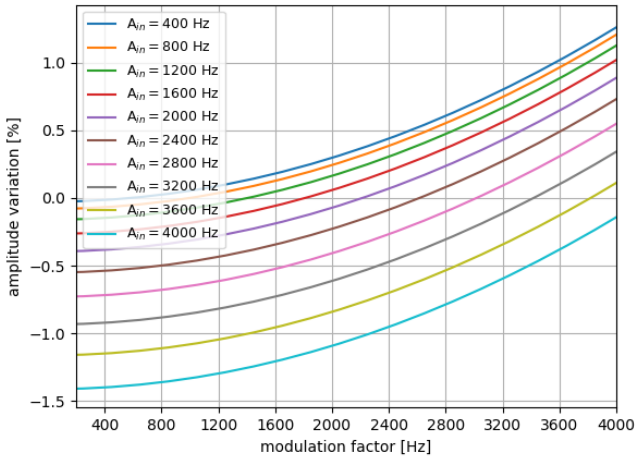**Figure 8.** Every curve is at different interferogram amplitude $(A_{in})$. Interferogram amplitude percentile variation $\left(\frac{A_{out}-A_{in}}{A_{in}}\right)$ vs modulation factor $(\Delta f_c)$. The background is fixed at zero. We can see how the error on the estimation converges to 0 when $\Delta f_c$ approaches $A_{in}$.

## 4.2. Validation on real data

In this subsection we show the results obtained from the commissioning campaign at the telescope. We can see in fig. 9 the circular fit performed on real data as described in fig. 4: the two external are the modulation points and the central distribution represents the variation of the signal during the observation.
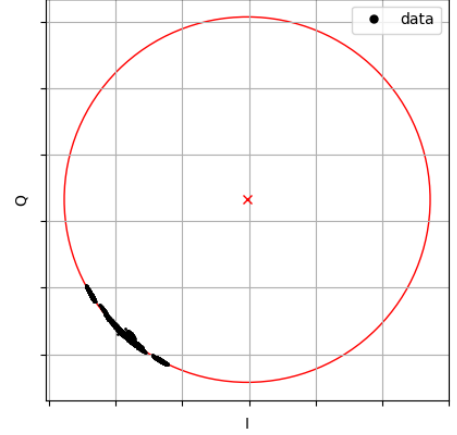


**Figure 9.** Observation in $(I, Q)$ plan: in black dots the data and in red shape the circular fit. We can see the two modulation (external) points and the central distribution due to the signal changing during the observation

Operatively, the circular fit showed in fig. 9 is used in two different ways and represents a crucial tool during the observations, as well as for the data analysis. Firstly, during the observation, it gives an important visual on-the-fly feedback to understand if the calibration is correctly working. Secondly, it is one of the first step in the conversion algorithm for the physical data analysis, as already described in subsec. 3.2.2.

The first result, that we can compare with the simulation, is reported in fig. 10: it is the calibration factor estimated as a function of TOI during a sky observation. Every point corresponds to a data block (sampled at 5 Hz).

Here we assume the background fluctuation, as seen in fig. 6, as unique source of incertitude for the calibration factor estimation: we consider the noise contamination negligible. Let's first demonstrate this assumption. Following the results in fig. 11 we take the median of the $ASD$ $(A\tilde{S}D)$ as its equivalent white noise level: it is, taking margins, ~1 $Hz/\sqrt{Hz}$.

We can, then, use the standard deviation definition of the TOI noise signal:

$$\sigma \doteq \int_0^{\Delta f} [ASD(f)]^2 \cdot df \,. \tag{13}$$

where $ASD(f)$ is the $ASD$ as a function of frequency $f \in [0, \Delta f]$, $\Delta f$ is the bandwidth equal to half of the sampling frequency (for the Nyquist theorem) and $df \doteq \Delta f/N$, where $N$ is the number of the points.

Approximating $ASD$ in eq. 13 as a pure white noise $(A\tilde{S}D)$ we obtain:

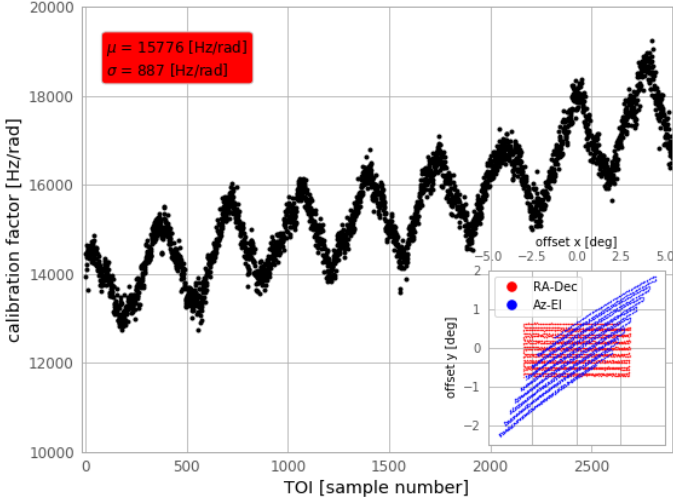$$\sigma \simeq \sqrt{A\tilde{S}D^2 \cdot \Delta f} \,, \tag{14}$$

**Figure 10.** Calibration factor as a function of TOI during an observation. The gaussian fit reported in the red top-left box is evaluated from the data that have been previously median filtered. We can notice the derive of the calibration factor due to the Right Ascension - Declination (RA-Dec) observation: the telescope increases the elevation following the source. In the bottom-right the offset maps of the sky-coordinates in both RA-Dec and Azimuth-Elevation (Az-El).
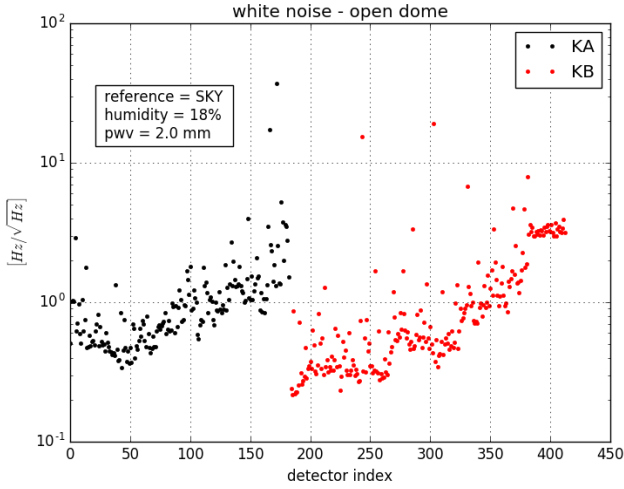


**Figure 11.** Equivalent white noise extrapolated from Amplitude Spectral Density ($ASD$). Every point is a pixel and they are represented different colours the two arrays $KA$ and $KB$. It is an observation with defocused sky as calibration source.

Finally, in tab. 2, we can see the typical fluctuations of the signal as a function of sampling rate: compared to the background variation (equivalent of $\sim 1$ kHz) simulation in fig. 10 it represents, Q.E.D., a very small components.

**Table 2.** From eq. 13 typical rounded-up 1-$\sigma$ noise signal.

| mode | bandwidth [Hz] | $\sigma$ [Hz] |
|---|---|---|
| single point | 1908 | ~50 |
| block data | 2 | ~2 |

Starting from this paradigm we can, thus, compare the results of the simulation with on sky observations. From the simulation we know that here is a $\lesssim 3\%$ variation of the calibration factor each kelvin background fluctuation, as shown in fig. 6. What we notice on sky (fig. 10) is a fluctuation $\sigma/\mu \sim 6\%$, where $\sigma$ is the standard deviation and $\mu$ the mean value of the calibration factor. We can conclude that during a typical $\sim 4$ degree scan we have temperature fluctuation of the sky $\lesssim 2$ K.

Secondly, what we need to state that the acquisition/data-reduction system is qualified for the instrument is to observe the capability of the calibration to adapt to different background (analogously to the autotuning of NIKA/NIKA2 described in subsec. 3.1.1). For this purpose, we take three consecutive maps at increasing elevation: we plot the $(I, Q)$ data of the first subscan for each map observing the behaviour of the acquisition referring the circular fit to the first tuning (corresponding to the first map). The result is shown in fig. 12.
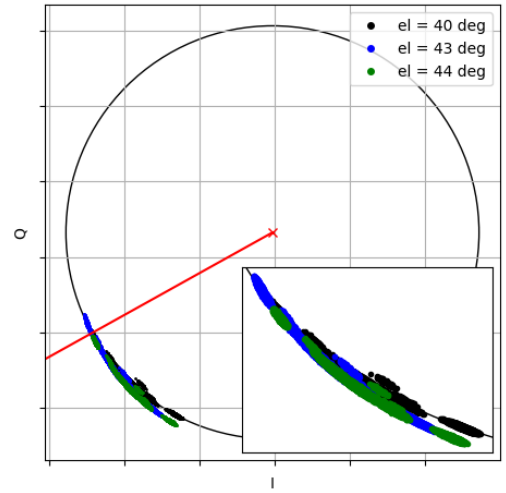


**Figure 12.** $(I, Q)$ signal of the first subscan for three consecutive maps, i.e., increasing elevation. The red straight line is the intercept between the origin and the circle centre.

We can see how the data are disposed on the same region close to the ones of the first circle, they are around the intercept between the centre of the circle the origin: it means that they are around the minimum of the resonance, i.e., to the frequency of resonance. The data are not perfectly centred because of the intrinsic incertitude on the binning of the injected tone. The radial shift is due to the background change: different elevations correspond to a different air mass ($\sim 1/\cos(el)$). The calibration technique performed between each map recovers the resonance tone, adapting it to the background change.

## 5. Conclusions and Perspectives

The purpose of this paper is to demonstrate and explain the new acquisition technique for KISS. As previously mentioned, this algorithm is naturally implementable for all those instruments that will aim to exploit KID-based interferometers: a worthwhile solution for the contemporary and future multi-wavelength cosmology. Although KISS represents a standalone instrument to make science, it opens future perspectives for larger arrays experiments, like CONCERTO Lagache (2019). Specifically for

these cases, in fact, our new algorithm will minimise the data production and contain the inflation on the electronics specifications.

## References

Adam, R., Adane, A., Ade, P. A. R., et al. 2018, , 609, A115

Calvo, M., Roesch, M., Désert, F.-X., et al. 2013, , 551, L12

Catalano, A., Adam, R., Adane, A., et al. 2014a, in , Vol. 9153, Millimeter, Submillimeter, and Far-Infrared Detectors and Instrumentation for Astronomy VII, 915302

Catalano, A., Calvo, M., Ponthieu, N., et al. 2014b, , 569, A9

Endo, A., Baselmans, J. J. A., van der Werf, P. P., et al. 2012, in Society of Photo-Optical Instrumentation Engineers (SPIE) Conference Series, Vol. 8452, , 84520X

Fasano, A. submitted-a, The European Physical Journal Web of Conferences

Fasano, A. submitted-b, Journal of Low Temperature Physics

Gao, J. 2008, The Physics of Superconducting Microwave Resonators

Lagache, G. 2019, people.lam.fr/lagache.guilaine/CONCERTO.html

Li, C.-T., Bradford, C. M., Crites, A., et al. 2018, in Society of Photo-Optical Instrumentation Engineers (SPIE) Conference Series, Vol. 10708, Millimeter, Submillimeter, and Far-Infrared Detectors and Instrumentation for Astronomy IX, 107083F

Martin, D. H. & Puplett, E. 1970, Infrared Physics, 10, 105

Mather, J. C., Fixsen, D. J., Shafer, R. A., Mosier, C., & Wilkinson, D. T. 1999, , 512, 511

Monfardini, A., Swenson, L. J., Bideaud, A., et al. 2010, , 521, A29

Swenson, L. J., Cruciani, A., Benoi, A., et al. 2010, Applied Physics Letters, 96, 263511

Zmuidzinas, J. 2012, Annual Review of Condensed Matter Physics, 3, 169